

Two energy scales of spin dimers in clinoclase $\text{Cu}_3(\text{AsO}_4)(\text{OH})_3$

Stefan Lebernegg,¹ Alexander A. Tsirlin,^{1,2,*} Oleg Janson,^{1,2} and Helge Rosner^{1,†}

¹*Max Planck Institute for Chemical Physics of Solids, Nöthnitzer Str. 40, 01187 Dresden, Germany*

²*National Institute of Chemical Physics and Biophysics, 12618 Tallinn, Estonia*

Magnetic susceptibility and microscopic magnetic model of the mineral clinoclase $\text{Cu}_3(\text{AsO}_4)(\text{OH})_3$ are reported. This material can be well described as a combination of two nonequivalent spin dimers with the sizable magnetic couplings of $J \simeq 700$ K and $J_{\text{D2}} \simeq 300$ K. Based on density functional theory calculations, we pinpoint the location of dimers in the crystal structure. Surprisingly, the largest coupling operates between the structural Cu_2O_6 dimers. We investigate magnetostructural correlations in Cu_2O_6 structural dimers, by considering the influence of the hydrogen position on the magnetic coupling. Additionally, we establish the hydrogen positions that were not known so far and analyze the pattern of hydrogen bonding.

PACS numbers: 75.30.Et, 75.50.Ee, 75.10.Jm, 91.60.Pn

I. INTRODUCTION

The majority of magnetic systems have more than one characteristic energy scale, according to the different nature of interactions between the spins. For example, in low-dimensional magnets strong interactions within chains or planes are of direct exchange or superexchange type, whereas weak interchain (interplane) couplings may have purely dipolar origin.^{1–3} The different energy scale of these interactions implies that, at sufficiently high temperatures, the magnetic behavior is solely determined by the strong couplings, and the system can be fully described in terms of a low-dimensional spin model.^{1,4} However, at low temperatures, interchain (interplane) couplings come into play, and a full three-dimensional description is required.

In complex spin systems, the identification of different energy scales is by no means a simple problem. Naively, one could think that distinct crystallographic positions of magnetic atoms should lead to different strengths of magnetic couplings and, therefore, to different energy scales of the magnetic behavior. Indeed, in spin-dimer systems, such as $\text{BaCuSi}_2\text{O}_6$ and NH_4CuCl_3 , the spin- $\frac{1}{2}$ Cu^{2+} ions occupy several nonequivalent positions^{5,6} and form different types of spin dimers which have large impact on the high-field behavior, including the unusual critical regime of the Bose-Einstein condensation of magnons in $\text{BaCuSi}_2\text{O}_6$ (Refs. 7) and the fractional magnetization plateaus in NH_4CuCl_3 (Refs. 8 and 9). However, spin dimers can also be formed between two nonequivalent Cu positions, thus leading to only one type of spin dimer and one energy scale, as in the spin-ladder compound BiCu_2PO_6 .¹⁰

When the system contains several Cu^{2+} positions with dissimilar local environment and variable connectivity of the Cu polyhedra, the identification of relevant interactions and energy scales becomes increasingly complex. The problem of magnetic dimers that do not match structural dimers,^{11–13} as well as magnetic chains running perpendicular to the structural chains,¹⁴ is well-known in quantum magnets and requires a careful microscopic

analysis.

Here, we report on the magnetic behavior and microscopic modeling of clinoclase, $\text{Cu}_3(\text{AsO}_4)(\text{OH})_3$. The intricate crystal structure of this mineral^{15,16} features three nonequivalent Cu positions. Nevertheless, the resulting spin lattice comprises only two types of magnetic dimers with notably different interaction energies. Our microscopic analysis shows that one spin dimer is formed between two different Cu positions (Cu1–Cu2) and does not match the respective structural dimer. However, the other spin dimer coincides with the Cu3–Cu3 structural dimer. We argue that neither a straightforward comparison of Cu–Cu distances nor the application of the Goodenough-Kanamori-Anderson (GKA) rules for the superexchange^{17–19} lead to the correct assignment of magnetic couplings in clinoclase. Therefore, all geometrical details of relevant exchange pathways should be taken into account and considered simultaneously. We elaborate on this problem by determining the positions of hydrogen atoms and analyzing their role in the superexchange.

The outline of the paper is as follows. Sec. II summarizes experimental and computational techniques that were applied in this study. In Sec. III A, we report details of the sample characterization followed by the determination of hydrogen positions and the discussion of the crystal structure in Sec. III B. Sec. III C presents experimental magnetic properties and their brief discussion in terms of a phenomenological model of two spin dimers with different energy scales, whereas Sec. III D provides a microscopic insight into this model and into residual interactions between the spin dimers. Finally, Sec. III E clarifies the role of hydrogen atoms in the Cu–O–Cu superexchange. Our work is concluded with a discussion and summary in Sec. IV.

II. METHODS

For our experimental studies, we used a natural sample of clinoclase from Wheal Gorland, St. Day United Mines (Cornwall, UK), which is the type locality of this rare

mineral. The sample provided by the mineralogical collection of Salzburg University (Department of materials engineering and physics) features bulky dark-blue crystals of clinoclase together with smaller light-blue crystals of liroconite, $\text{Cu}_2\text{Al}(\text{AsO}_4)(\text{OH})_4 \cdot 4(\text{H}_2\text{O})$. The crystals of clinoclase were manually separated from foreign phases and carefully analyzed by powder x-ray diffraction (XRD) and chemical analysis. Laboratory powder x-ray diffraction (XRD) data were collected using the Huber G670 Guinier camera ($\text{CuK}_{\alpha 1}$ radiation, ImagePlate detector, $2\theta = 3-100^\circ$ angle range). Additionally, high-resolution XRD data were collected at the ID31 beamline of the European Synchrotron Radiation Facility (ESRF, Grenoble) at a wavelength of about 0.43 Å. The chemical composition was determined by the ICP-OES method.²⁰ The thermal stability of clinoclase was investigated by thermogravimetric analysis²¹ up to 500 °C.

Magnetic susceptibility of clinoclase was measured with a Quantum Design MPMS SQUID magnetometer in the temperature range of 2 – 380 K in fields up to 5 T.

Electronic structure calculations were performed within density functional theory (DFT) by using the full-potential local-orbital code FPLO9.07-41.²² Local density approximation (LDA)²³ and generalized gradient approximation (GGA)²⁴ were used for the exchange-correlation potential, together with a well converged k -mesh of $6 \times 6 \times 6$ points for the crystallographic unit cell of clinoclase and about 100 points in supercells. Hydrogen positions missing in the presently available crystallographic data^{15,16} were obtained by structural optimizations with a threshold for residual forces of 0.002 eV/Å.

The effects of strong electronic correlations, typical for cuprates, were considered by mapping the LDA bands onto an effective tight-binding (TB) model. The transfer integrals t_i of the TB-model are evaluated as non-diagonal matrix elements in the basis of Wannier functions (WFs). These transfer integrals t_i are further introduced into the half-filled one-orbital Hubbard model $\hat{H} = \hat{H}_{TB} + U_{\text{eff}} \sum_i \hat{n}_{i\uparrow} \hat{n}_{i\downarrow}$ that is eventually reduced to the Heisenberg model for the low-energy excitations,

$$\hat{H} = \sum_{\langle ij \rangle} J_{ij} \hat{S}_i \cdot \hat{S}_j, \quad (1)$$

where the summation is done over bonds $\langle ij \rangle$. For the half-filled case, which applies to clinoclase, the reduction to the Heisenberg model is well-justified in the strongly correlated limit $t_i \ll U_{\text{eff}}$, with the effective on-site Coulomb repulsion U_{eff} exceeding t_i by at least an order of magnitude (see Table II). This procedure yields AFM contributions to the exchange coupling evaluated as $J_i^{\text{AFM}} = 4t_i^2/U_{\text{eff}}$.

Alternatively, full exchange couplings J_i , comprising FM and AFM contributions, can be derived from differences in total energies of various collinear spin arrangements, as evaluated in spin-polarized supercell calculations within density functional theory LSDA+ U formalism that includes a mean-field correction for correlation effects. An “around mean field” (AMF) as well as a

“fully localized limit” (FLL) approximation for correcting the double counting were used.²⁵ Both types supplied consistent results so that only the AMF results are presented here. The on-site Coulomb repulsion and on-site Hund’s exchange of the Cu 3*d* orbitals are chosen as $U_d = 6.5 \pm 0.5$ eV and $J_d = 1$ eV, respectively, according to the parameter set used for several other cuprates.²⁶⁻²⁸

In addition to periodic DFT calculations, we performed a series of cluster calculations that pinpoint the effect of hydrogen atoms on the superexchange. The cluster under consideration is based on the $\text{Cu}_2\text{O}_6\text{H}_5$ dimer and embedded in a set of point charges, with two As ions bonded to the dimer considered as total ion potentials (TIPs).^{29,30} The embedding was chosen so that the intradimer hopping obtained from the cluster and periodic LDA calculations match. The cluster calculations were done with the ORCA 2.9 code^{31,32} in combination with a 6-311++G(d,p) basis set and a PBE0 hybrid functional.³³

Quantum Monte Carlo (QMC) and simulations were performed using the codes LOOP³⁴ and DIRLOOP_SSE³⁵ from the software package ALPS-1.3.³⁶ Magnetic susceptibility was simulated on finite lattices of $N=2400$ spins $S = \frac{1}{2}$, using 40 000 sweeps for thermalization and 400 000 sweeps after thermalization. For simulations of magnetization isotherms, we used 4000 sweeps for thermalization and 40 000 sweeps after thermalization. Magnetization of the “2+1” model was simulated using the full diagonalization code from ALPS-1.3.³⁶

III. RESULTS

A. Sample characterization

Powder XRD confirmed the purity of our clinoclase sample. However, the ICP-OES analysis showed slight deviations from the ideal composition: 49.6(3) wt.% Cu, 18.3(1) wt.% As compared to 50.1(1) wt.% Cu, 19.7(1) wt.% As expected for $\text{Cu}_3(\text{AsO}_4)(\text{OH})_3$. Additionally, trace amounts of Ca and S (0.1–0.2 wt.%) were found. Other detectable elements, including transition metals, are below 0.03 wt.%.

To verify the composition of the clinoclase phase, we performed structure refinement using high-quality synchrotron data collected at room temperature. The lattice parameters we obtained for the space group $P2_1/c$ are $a = 7.266$ Å, $b = 6.459$ Å, $c = 12.393$ Å with the monoclinic angle $\beta = 99.49^\circ$. They agree well with the existing single-crystal data,¹⁶ where $a = 7.257$ Å, $b = 6.457$ Å, $c = 12.378$ Å and $\beta = 99.51^\circ$, which we used for the magnetic modeling. Our refinement confirmed full occupation of all atomic positions in the clinoclase structure.³⁷ As Cu and As are the two heaviest elements (and, therefore, strongest scatterers) in $\text{Cu}_3(\text{AsO}_4)(\text{OH})_3$, their content in the crystalline phase is safely established by XRD. Regarding the bulk composition, the slight deficiency of Cu and As, as revealed by chemical analysis, may be

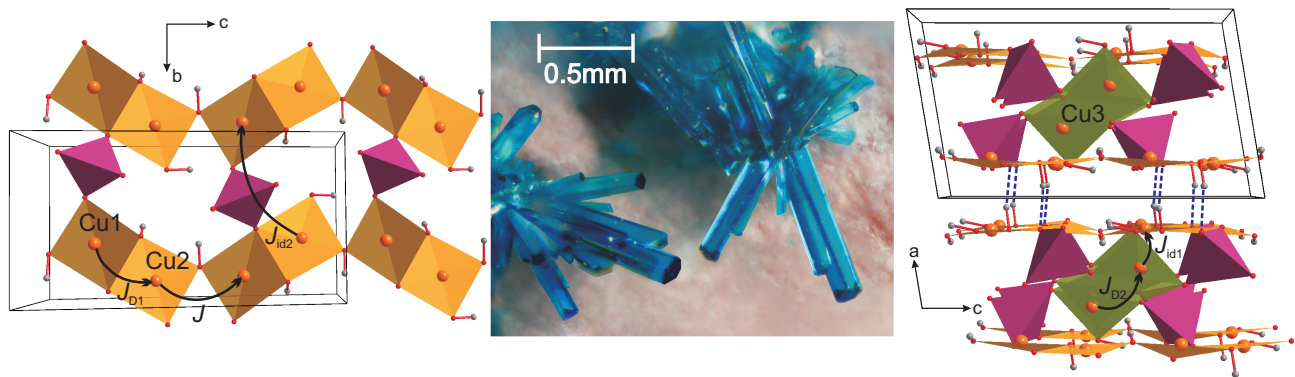


FIG. 1. (Color online) The crystal structure of clinoclase. The D1 (Cu1–Cu2) structural dimers are shown in orange, the D2 (Cu3–Cu3) dimers in greenish color. The left panel shows a single layer consisting of zig-zag chains of D1-dimers linked by AsO_4 tetrahedra (pink). In the right panel, the sandwich-like structure of clinoclase is visible with the hydrogen bonds shown as (blue) dashed lines. Arrows indicate the leading hopping pathways. The central panel shows high-quality natural clinoclase crystals from the Majuba Hill Mine, Pershing Co., Nevada, USA.

attributed to trace amounts of secondary phases, such as CaCO_3 and CaSO_4 that are possible impurities in natural samples. Another plausible impurity is CuO (tenorite), which is difficult to identify by XRD, because its strongest reflections overlap with those of clinoclase. Note that none of the possible impurities reveal any conspicuous effects in the magnetic susceptibility and should not affect our experimental results reported in Sec. III C.

Thermogravimetric analysis (TGA) identified the onset of the decomposition at about 180°C and the weight loss of 7.1% upon heating to 500°C .³⁷ This weight loss implies the release of 1.5 water molecules per formula unit, as expected for $\text{Cu}_3(\text{AsO}_4)(\text{OH})_3$. The sample recovered after the heating contained a mixture of unknown phases. Their composition and crystal structures require further investigation that lies beyond the scope of the present study.

B. Crystal structure

Clinoclase crystallizes in the monoclinic space group $P2_1/c$ and forms a fairly complex crystal structure with three nonequivalent Cu positions (Fig. 1).¹⁶ All Cu sites have a five-fold square-pyramidal coordination, where the four oxygen atoms in the basal plane form shorter bonds to Cu (1.9–2.1 Å), whereas the distance to the axial oxygen atom is above 2.3 Å. Similar to other cuprates, superexchange pathways and ensuing magnetic interactions can be described by resorting to the planar CuO_4 coordination, because the oxygen atom in the axial position of the pyramid does not take part in the superexchange (see Sec. III D).

The CuO_4 plaquettes around the Cu1 and Cu2 sites form doubly bridged dimers (D1 = Cu1–Cu2) that share corners and build zigzag chains directed along [001]. The AsO_4 tetrahedra connect these chains into layers in the bc plane. Two layers of this type form a “sandwich”

encompassing the dimers of Cu3 atoms (D2 = Cu3–Cu3). Although both D1 and D2 dimers are built of two CuO_4 plaquettes sharing a common edge, their symmetries and geometrical parameters are different. For example, the inversion symmetry in the center of D2 entails two equal Cu3–O–Cu3 angles. In contrast, D1 has no symmetry elements, hence its two Cu1–O–Cu2 bridging angles are not equal.

The connections between the “sandwiches” are restricted to hydrogen bonds and to long Cu–O bonds in the axial positions of the CuO_5 pyramids. This weak interlayer bonding is responsible for the perfect cleavage of clinoclase crystals parallel to (100), and for the low (Mohs)-hardness of 2.5–3 in this material.³⁸

Previous structure determinations^{15,16} were based on XRD data and did not report the positions of hydrogen atoms. However, precise positions of all atoms, including hydrogen, are required for DFT band structure calculations and ensuing microscopic analysis of the electronic and magnetic structure. Therefore, we determined the hydrogen positions by relaxing the crystal structure of clinoclase. Only the hydrogen positions were optimized, whereas all other atoms were fixed to their experimental positions.³⁹ In the starting model, hydrogens were attached to three out of seven oxygen atoms at a typical O–H distance of 1.0 Å. The orientation of the O–H bonds was random, although we made sure that the hydrogens are well separated from other atoms in the clinoclase structure. While there is freedom in choosing three oxygen atoms forming covalent bonds to hydrogen, only those oxygens that do not belong to the AsO_4 tetrahedra led to structures with low energies. When hydrogens are attached to oxygens belonging to the AsO_4 tetrahedra, the energy is much higher, hence such structures can be ruled out. This is in agreement with the empirical assignment of the OH groups in the experimental crystallographic study.¹⁶

The resulting hydrogen positions are listed in Table I.

TABLE I. Hydrogen positions obtained by LDA/GGA structure optimization. The positions of oxygen forming short O–H bonds to these hydrogen atoms are given in brackets.

atom	x/a	y/b	z/c
H1 (O5)	0.7429/0.7493	0.3513/0.3515	0.4799/0.4807
H2 (O6)	0.9362/0.9346	0.4685/0.4680	0.6792/0.6786
H3 (O7)	0.1522/0.1511	0.1635/0.1648	0.4876/0.4864

Further details of the relaxation procedure and comparisons to the experiment for other Cu^{2+} hydroxy-salts can be found in Refs. 26 and 40. The optimized O–H distances are close to 1.0 Å, as expected for the covalent O–H bonds. Each hydrogen atom also forms one longer contact of about 1.8 Å (hydrogen bond) to another oxygen atom. Two of these contacts provide additional bonding within the layer,³⁷ whereas the hydrogen bond formed by H2 connects adjacent “sandwiches” (see Fig. 1). This arrangement of hydrogen bonds correlates with the positions of the hydrogens: while H1 and H3 are nearly coplanar with Cu and O atoms, H2 is notably shifted along the a direction toward the neighboring “sandwich”. Therefore, H1 and H3 lie in the plane of the D1 dimer plaquettes, whereas H2 and the respective O–H bond are in the out-of-plane position.

C. Magnetization measurements and phenomenological fits

The temperature dependence of the magnetic susceptibility $\chi(T)$ is shown in Fig. 2. In quantum magnets, $\chi(T)$ typically has an asymmetric dome-like shape, with a broad maximum indicating a gradual crossover from the high-temperature (paramagnetic) to the low-temperature (correlated) regime. Due to the unusually high magnetic energy scale in clinoclase, this maximum is shifted to high temperatures (~ 300 K) and is barely visible in the data collected below and around room temperature. Unfortunately, high-temperature measurements are not possible because the decomposition of clinoclase starts at about 450 K.³⁷

The upturn in $\chi(T)$ below 50 K is a typical extrinsic feature caused by defects and/or impurities. It can be reasonably described by a Curie-Weiss law with $C_{\text{imp}} = 0.015 \text{ emu K/mol}$, corresponding to 3.2% of $S = \frac{1}{2}$ impurities per f. u., and $\theta_{\text{imp}} = 2.5 \text{ K}$. After subtraction of the extrinsic contribution, we obtain vanishingly small susceptibility below 30 K and an activated (exponential) behavior at higher temperatures, evidencing the gapped nature of the magnetic excitation spectrum.

The gap between the lowest-lying $S = 0$ and $S = 1$ states (the spin gap) is inherent to numerous magnetic models. The simplest one is a quantum-mechanical spin dimer with a singlet ground state. Indeed, the structure of clinoclase features well-defined structural dimers D1

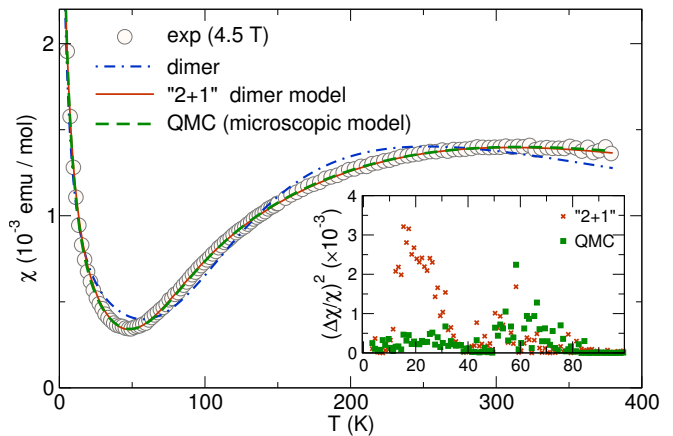


FIG. 2. Experimental magnetic susceptibility (circles) of clinoclase $\text{Cu}_3(\text{AsO}_4)(\text{OH})_3$ and fits using a dimer model (dash-dotted line), the phenomenological model [Eq. 3] of 2+1 dimers (solid line), and the microscopic model of coupled spin dimers, as shown in Fig. 8 (dashed line, QMC fit). Besides the intrinsic dimer susceptibility [Eq. 2], we accounted for the temperature-independent contribution and a Curie-Weiss impurity and/or defect contribution. Inset: difference curves for the 2+1 dimers solution and the QMC fit.

and D2 that are evocative of the spin-dimer magnetism. For a system of isolated dimers, the magnetic susceptibility is given by the exact analytical expression:

$$\chi(T) = \frac{Ng^2\mu_B^2}{T} \frac{1}{(3 + \exp[J/T])}, \quad (2)$$

where J is the magnetic exchange within the dimer. The fit yields $J = 415 \text{ K}$, but it does not account for the shape of the experimental curve, as shown in Fig. 2. Moreover, the resulting value of the g -factor ($g = 1.48$) is unrealistically small for Cu^{2+} .

The failure of the isolated dimer model suggests that the magnetic couplings in clinoclase are more intricate. Prior to the microscopic evaluation (Sec. III D), we attempt to describe the $\chi(T)$ dependence with a phenomenological magnetic model. According to Sec. III B, the monoclinic unit cell of clinoclase contains three structural dimers formed by edge-sharing CuO_4 plaquettes (Fig. 1). Two of these dimers are of the D1 type (Cu1–Cu2), whereas the third dimer is D2 (Cu3–Cu3). Naturally, the magnetic couplings within D1 are different from those in D2. This brings us to a tentative model of 2+1 dimers:

$$H = 2H_{\text{D1}} + H_{\text{D2}} \quad (3a)$$

$$H_{\text{D1}} = \frac{1}{2} \sum_{\substack{i \in \text{Cu1} \\ j \in \text{Cu2}}} J_{\text{D1}}(\mathbf{S}_i \cdot \mathbf{S}_j) \quad (3b)$$

$$H_{\text{D2}} = \sum_{\langle i,j \rangle \in \text{Cu3}} J_{\text{D2}}(\mathbf{S}_i \cdot \mathbf{S}_j), \quad (3c)$$

where J_{D1} and J_{D2} denote the magnetic couplings in the respective dimers. For each dimer, the magnetic susceptibility is given by Eq. (2).

Two scenarios are possible: either $J_{D1} > J_{D2}$, or the other way around. Fitting to the experimental curve readily shows that the $J_{D2} > J_{D1}$ solutions do not reproduce the experimental behavior. In contrast, the model with $J_{D1} > J_{D2}$ yields an excellent fit with $J_{D1} = 703.5$ K $J_{D2} = 289.3$ K, and $g = 1.86$ (full line in Fig. 2). Therefore, the smaller gap of ~ 290 K comes from the Cu3–Cu3 dimers (D2), while the Cu1–Cu2 dimers (D1) give rise to the larger gap of ~ 700 K.

D. Microscopic magnetic model

Now, we compare the above phenomenological model with the microscopic results based on DFT. In a first step, LDA calculations are performed. The width of the whole valence band block of about 9 eV is typical for cuprates (see Fig. 3). The spurious metallicity of the energy spectrum is a well-known shortcoming of LDA due to the underestimated electronic correlation in the Cu 3d shell.⁴¹ Nevertheless, the LDA bands around the Fermi level (the energy range from -0.5 to 0.7 eV) are sufficient to describe low-energy magnetic excitations, provided that a suitable correlation part is added to the model Hamiltonian. The relevant bands are essentially of the Cu d_{xy} character, with sizable contributions from O $2p$ orbitals. The orbital symmetry is defined with respect to the local coordinate system on each CuO_4 -plaquette, where the Cu–Cu bond of the dimer is chosen as the local x -axis, and the z -axis is orthogonal to the plaquette plane. Note that this setting is different from the standard one, where x and y axes are directed along the Cu–O bonds, so that the highest crystal-field level has the $d_{x^2-y^2}$ symmetry.

The leading hopping parameters t_i and corresponding AFM exchanges $J_i^{\text{AFM}} = 4t_i^2/U_{\text{eff}}$ are listed in Table II. The results of the model analysis are supported by the evaluation of full exchange integrals J_i using total energies of collinear spin configurations calculated with LSDA+ U . These two approaches are complementary. The model analysis provides information on all exchange couplings in the system and guides the LSDA+ U calculations that are restricted to only a handful of leading interactions.

Our model analysis based on the hopping parameters t_i identifies five leading AFM exchanges that exceed 100 K (see J_i^{AFM} in Table II). The perfect agreement between the LDA bands at the Fermi level and those calculated with the Cu-centered Wannier functions (Fig. 3) confirms that the relevant superexchange pathways in clinoclase can be well described in terms of the CuO_4 plaquettes. Despite the short Cu–Cu distance of only 3.3 Å between the Cu atoms in two contiguous “sandwiches” along the a direction, the respective hopping is negligibly small (below 20 meV) because the magnetic orbitals lie in the bc plane and do not overlap. Likewise, two outer layers of each “sandwich” are coupled only via the Cu3 spins and lack any direct interaction.

The comparison between J_i^{AFM} and J_i in Table II

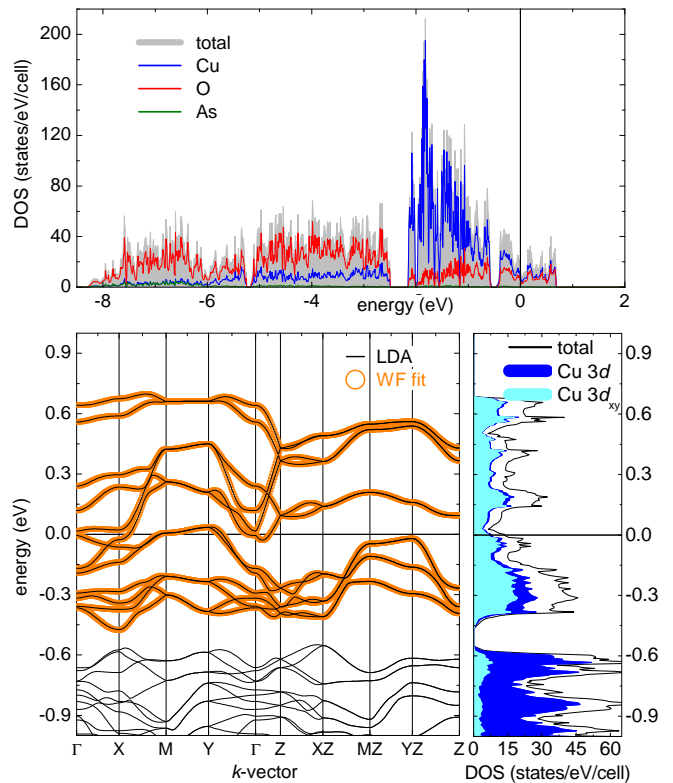


FIG. 3. (Color online) The LDA density of states (DOS) and the band structure of clinoclase $\text{Cu}_3(\text{AsO}_4)(\text{OH})_3$. The top panel shows the contributions of the Cu(3d), O(2p) and As states to the total DOS. The Fermi level is at zero energy. In the bottom left panel, the LDA-bands around the Fermi level are displayed and compared with bands derived from a fit using an effective one-band tight-binding model based on Cu-centered Wannier functions (WFs) projected on local Cu($3d_{xy}$)-orbitals. The k -points are defined as follows: $\Gamma = (000)$, $X = (\frac{\pi}{a}00)$, $Y = (0\frac{\pi}{b}0)$, $Z = (00\frac{\pi}{c})$, $XZ = (\frac{\pi}{a}0\frac{\pi}{c})$, $MZ = (\frac{\pi}{a}\frac{\pi}{b}\frac{\pi}{c})$, $YZ = (0\frac{\pi}{b}\frac{\pi}{c})$. The bottom right panel shows that the partial Cu(3d)-DOS at the Fermi level is basically of Cu($3d_{xy}$) character, justifying our construction of the WFs.

TABLE II. Leading exchange couplings in clinoclase $\text{Cu}_3(\text{AsO}_4)(\text{OH})_3$: Cu–Cu distances $d_{\text{Cu–Cu}}$ (in Å), bridging angles $\varphi_{\text{Cu–O–Cu}}$ (in deg), hopping integrals t_i (in meV), antiferromagnetic contributions $J_i^{\text{AFM}} = 4t_i^2/U_{\text{eff}}$ (in K) with $U_{\text{eff}} = 4.0$ eV. The J_i (in K) are calculated with LSDA+ U using $U_d = 6.5 \pm 0.5$ eV, $J_d = 1$ eV.

	$d_{\text{Cu–Cu}}$	$\varphi_{\text{Cu–O–Cu}}$	t_i	J_i^{AFM}	J_i
J_{D1}	2.98	93.6/99.9	–115	153	-4 ± 8
J_{D2}	3.13	101.9	191	423	302 ± 53
J_{id1}	3.38	124.6	–117	159	161 ± 25
J	3.66	149.3	276	884	693 ± 99
J_{id2}	5.52	–	–106	130	159 ± 31

shows that four out of five leading interactions are indeed AFM, with only small FM contributions. However, the coupling within D1 is nearly canceled because of comparable FM and AFM terms. The large FM contribution to J_{D1} ($J_{D1}^{\text{FM}} = J_{D1} - J_{D1}^{\text{AFM}} \simeq -160$ K) is indeed expected for the coupling geometry with bridging angles close to 90° .

Our microscopic model is consistent with the phenomenological analysis that suggested spin dimers with two different energy scales (Sec. III C). The coupling on D2 is $J_{D2} = 302$ K very close to 300 K found experimentally. However, the magnetic dimer with the coupling of about 700 K has to be re-assigned. The coupling within D1 is in fact very weak, so that the spin dimer with $J \simeq 700$ K is formed not on the Cu1–Cu2 structural dimer D1, but between the respective dimers, where the CuO_4 plaquettes share a common corner instead of sharing a common edge. This effect can be well understood in terms of the GKA rules for the superexchange, because the Cu–O–Cu angle for J is nearly 150° compared to only $93 - 100^\circ$ for J_{D1} . However, the GKA rules do not account for the fact that $J_{D2} \simeq 302$ K exceeds $J_{id1} \simeq 159$ K, even though the bridging angle for J_{D2} is notably smaller. This unusual behavior is further discussed in the next sections.

The re-assignment of the magnetic dimer has no effect on the fit of the magnetic susceptibility presented in Sec. III C since it is independent of the position of the dimers in the crystal structure. The interdimer couplings J_{id1} and J_{id2} are non-frustrated and can be taken into account by QMC. The resulting fit shown in Fig. 2 is only slightly better than the fit with the phenomenological “2+1” model. We find $J = 706.8$ K, $J_{D2} = 318.1$ K and $g = 1.893$ in good agreement with our previous results. The coupling between the magnetic dimers were chosen as $J_{id1} = J_{id2} = 0.125 J$ to yield best agreement with the experimental curve.

E. Role of hydrogen

One important difference between the coupling pathways for J_{D1} , J_{D2} , and J_{id1} pertains to the positions of hydrogen atoms. While the bridging oxygen atoms of D2 belong to the AsO_4 tetrahedra and have only weak contacts to hydrogen, the bridging atom for J_{id1} , as well as one of the bridging atoms of D1, form covalent O–H bonds. For studying the role of the O–H bonds in more detail, we will focus on the D1 dimer where, according to the very small exchange coupling and the planar Cu_2O_6 geometry, we expect interesting effects, as, e.g., a change from FM to AFM coupling.

The effect of the out-of-plane angle τ of the O–H bond on the intradimer coupling was studied by Ruiz *et al.*⁴² for small organic ligands. They found that a large τ (out-of-plane position of hydrogen) favors FM coupling. We attempted to verify this effect for the D1-dimer in clinoclase. In a first step, the t_{D1} hopping parameters are

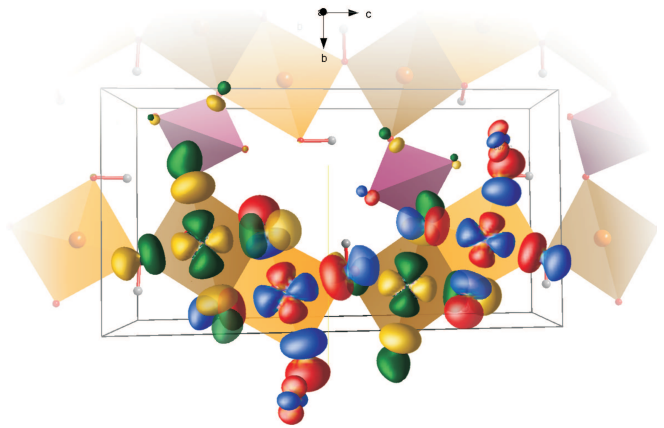


FIG. 4. (Color online) Wannier functions (WFs) on the Cu1 (yellow-green) and Cu2 sites (red-blue). The net overlap at the two bridging oxygen within the D1 dimers is significantly smaller than the overlap at the oxygen bridging two dimers. The Cu1-WF exhibits a considerable distortion towards the AsO_4 -tetrahedra responsible for the large J_{id2} coupling.

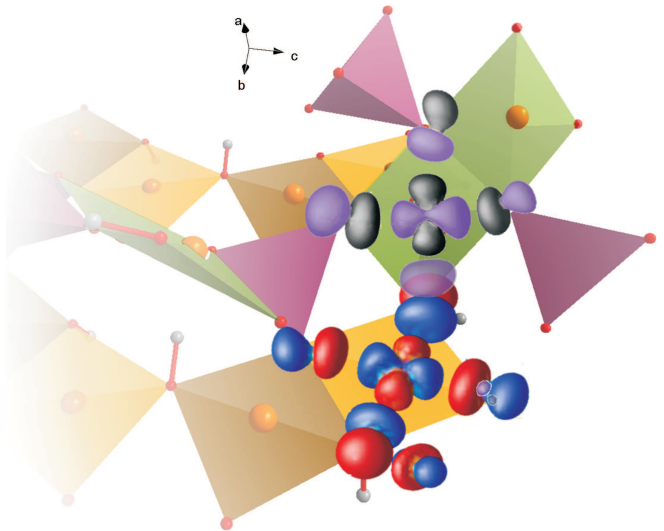


FIG. 5. (Color online) Wannier functions (WFs) on the Cu2 (red-blue) and Cu3 (grey-violet). The overlap between Cu2 and Cu3 is hampered by the non-planar arrangement of the CuO_4 plaquettes. The Cu3-WF features distortions of the $\text{O}(2p)$ contributions caused by the AsO_4 tetrahedra.

calculated as a function of τ in the periodic model. The out-of-plane rotation of H up to 67° , which corresponds to the optimized crystal structure of clinoclase, reduces t_{D1} by about 40% and, thus, the AFM contribution to J_{D1} by about 60% (see Supplemental material³⁷). Furthermore, t is slightly reduced and the inter-sandwich hoppings decrease by about 50%. All other hoppings are more or less independent of τ .

For the calculation of J_{D1} as a function of τ , we used the $\text{Cu}_2\text{O}_6\text{H}_5$ cluster model, embedded in TIPs and point charges, which allows to investigate the intradimer cou-

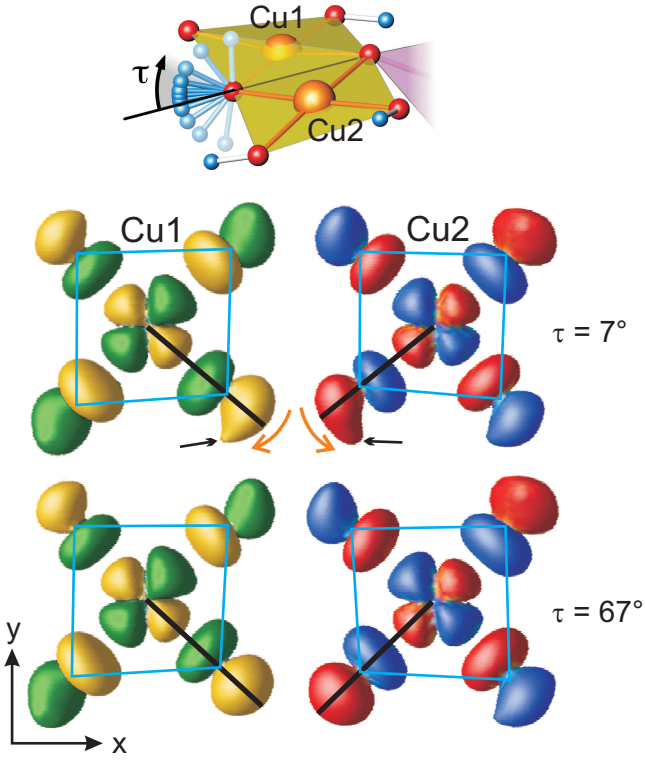


FIG. 6. (Color online) The effect of the out-of-plane rotation of hydrogen on the Wannier functions (WFs) localized at the Cu1 and Cu2 sites. The top figure shows the D1 structural dimer with H, bonded to the bridging oxygen, being rotated out of the dimer plane by an angle τ . The central and bottom figures show the WF at the two Cu sites for $\tau = 7^\circ$ and $\tau = 67^\circ$, respectively. The CuO_4 plaquettes are indicated in light blue, black lines connect the central Cu and the O bonded to H. With increasing τ , the $\text{O}(2p)$ orbital rotates (indicated by orange arrows) about a local z -axis, which is visible with respect to the black line. Black arrows point at the $\text{H}(1s)$ contribution to the WFs. At $\tau = 67^\circ$ that corresponds to the computationally relaxed structure, no such contributions are visible anymore.

pling exclusively. Additionally, the cluster enables us to vary the bridging angles without changing the whole set of additional structural parameters, as this would be the case for a periodic model.⁴³

The results of the cluster calculations (Fig. 7) nicely show the transition from AFM to FM coupling upon an increase in τ . This effect is driven by the reduced hopping, because the FM contribution $J_{\text{D1}}^{\text{FM}} = J_{\text{D1}} - J_{\text{D1}}^{\text{AFM}}$ is weakly dependent on τ and hovers around -150 K. The absolute size of J_{D1} obtained in the cluster calculations with the PBE0 functional is somewhat larger than the LSDA+ U estimates. This is in fact little surprising, because hybrid functionals, such as PBE0, tend to overestimate the exchange couplings.³⁰

The decrease in t_{D1} can be traced back to the increasing contribution of the bridging oxygen $\text{O}(2p_y)$ to the WFs of the Cu1 and Cu2 sites (Fig. 7), while the $\text{O}(2p_x)$ contribution remains constant. At small τ , $\text{H}(1s)$

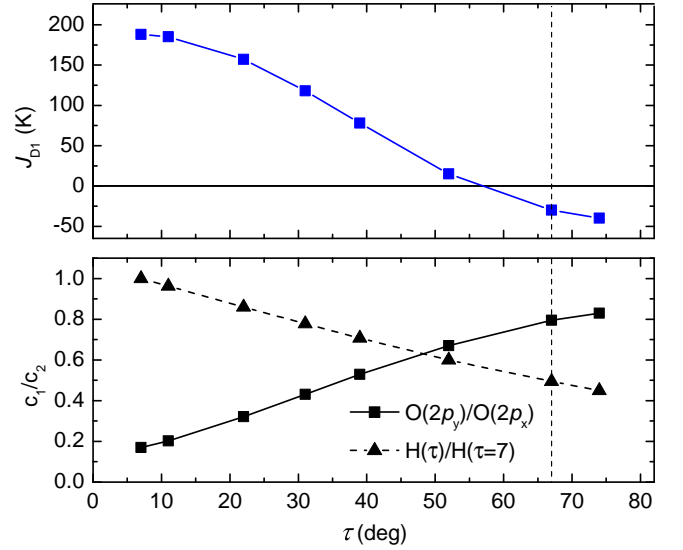


FIG. 7. (Color online) The upper panel shows J_{D1} as a function of the out-of-plane angle of hydrogen, τ . In the lower panel, the ratio $\text{O}(2p_y)/\text{O}(2p_x)$ of the WF-contributions of the bridging oxygen bonded to H are displayed. The orbital character is denoted with respect to the coordinate system shown in Fig. 6. $\text{H}(\tau)/\text{H}(\tau=7)$ shows the $\text{H}(1s)$ contribution normalized to the value at $\tau = 7^\circ$. The vertical dashed line indicates the computationally relaxed out-of-plane angle of hydrogen.

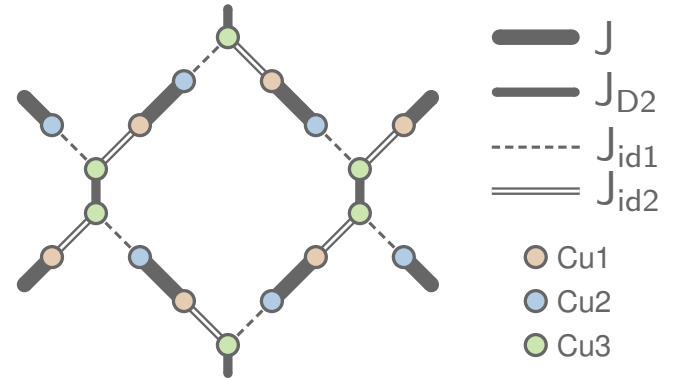


FIG. 8. Microscopic magnetic model of clinoclase $\text{Cu}_3(\text{AsO}_4)(\text{OH})_3$. Note that each structural “sandwich” depicted in Fig. 1 comprises three interpenetrating lattices of this type that are decoupled from each other. For the notation of magnetic couplings, see Table II.

strongly interacts with $\text{O}(2p_y)$ and thus shifts its orbital energy downwards, which in turn reduces the interaction between this oxygen orbital and $\text{Cu}(3d_{xy})$ orbitals. The $\text{H}(1s)$ contribution itself decreases with increasing τ . This is also visible in the WF-picture (Fig. 6) as the rotation of the contribution of bridging oxygen atoms. As the τ increases, the $\text{O}(2p)$ orbital turns into the direction perpendicular to the Cu–Cu axis of D1, hence the overlap of the WF’s of Cu1 and Cu2 is reduced.

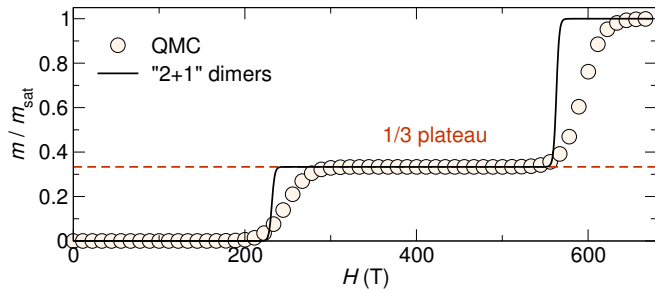


FIG. 9. Magnetization isotherm of clinoclase $\text{Cu}_3(\text{AsO}_4)(\text{OH})_3$ simulated using exact diagonalization of the “2+1” dimers model and QMC for the microscopic magnetic model with $J : J_{D2} : J_{id1} : J_{id2} = 1 : 0.45 : 0.125 : 0.125$. Magnetic field is scaled adopting J and g values from the $\chi(T)$ fits (Fig. 2). m_{sat} is the saturation magnetization. Note two wide plateaus at $m/m_{\text{sat}} = 0$ and $m_{\text{sat}} = 1/3$.

IV. DISCUSSION

The magnetism of clinoclase is well described by a model of two nonequivalent spin dimers. While this model is easily derived from the crystal structure of the mineral (Sec. III C), the arrangement of magnetic dimers cannot be established on purely empirical grounds. Two shortest Cu–Cu distances are formed within the structural dimers D1 and D2. Assuming that the magnetic coupling is more efficient at short distances, one would identify these structural dimers as magnetic dimers. This assessment is correct for D2, yet it fails for D1, where the strong interaction J forming the magnetic dimer is found between the structural D1 dimers. The GKA rules could provide a more plausible scenario, because they account for the fact that short Cu–Cu distances entail Cu–O–Cu angles close to 90° that are unfavorable for an AFM coupling. The reference to the GKA rules readily explains why the dimer is formed by J (bridging angle of 149.3°) and not by J_{D1} (bridging angles below 100°). However, a consistent application of these rules would also relegate J_{D2} (101.9°) that should be well below J_{id1} with a much larger Cu–O–Cu angle of 124.6° .

In clinoclase, neither Cu–Cu distances nor Cu–O–Cu angles fully elucidate the microscopic scenario. To explain why J_{D2} exceeds J_{id1} , details of their superexchange pathways should be analyzed and compared. Apart from the hydrogen atoms considered in Sec. III E, we find two main differences between these couplings: i) the number of bridging oxygen atoms, which is two for J_{D2} and one for J_{id1} ; ii) the mutual arrangement of the CuO_4 plaquettes that are coplanar for J_{D2} and strongly twisted for J_{id1} . Dividing the overall Cu–Cu hopping t_{D2} by two, we obtain $t_{D2}^{\text{eff}} = 95$ meV that reflects the transfer via a single Cu–O–Cu bridge (as in J_{id1}). This hopping is slightly below $|t_{id1}| = 117$ meV, but their difference is much smaller than expected for the bridging angles of 101.9° and 124.6° , respectively. For example, the model calculation from Ref. 44 suggests that t_{id1} should be at

least twice larger than t_{D2} .

There are different scenarios explaining the large AFM coupling of J_{D2} : It may originate from the combined effect of the indirect Cu–O–Cu and direct Cu–Cu hoppings within the Cu_2O_6 structural dimer. While the Cu–O–Cu processes should be solely determined by the bridging angle, the direct hopping requires the coplanar arrangement of the CuO_4 plaquettes, which is the case for J_{D2} only. This explanation is in line with the robust AFM coupling observed in many other spin-dimer compounds, such as TlCuCl_3 (Ref. 45) and $\text{SrCu}_2(\text{BO}_3)_2$ (Ref. 46), despite their low bridging angles of $96 - 98^\circ$. Same arguments could be applied to D1, where one of the bridging angles is as large as 100° and indeed leads to a sizable transfer $t_{D1} = -115$ meV. However, the out-of-plane O–H bond (see Sec. III E) has strong impact on the superexchange and is responsible for the very weak coupling. This effect of side groups may also play an important role for D2, yet in a different manner. Here, the bridging oxygen atoms belong to the AsO_4 tetrahedra that could amplify the AFM superexchange, similar to GeO_4 tetrahedra in CuGeO_3 .⁴⁷ Note that the structural dimers in $\alpha\text{-Cu}_2\text{As}_2\text{O}_7$ (bridging angle of 101.7°) are very similar to D2 and also feature a strong AFM coupling.^{12,48}

Another interesting feature of clinoclase is the sizable interdimer coupling J_{id2} . In contrast to all magnetic couplings discussed so far, J_{id2} does not involve a direct connection between the CuO_4 plaquettes and occurs via the bridging AsO_4 tetrahedron. The efficiency of this superexchange pathway can be explained by the coplanar and, moreover, well aligned arrangement of the CuO_4 plaquettes. Their positions are such that two Cu–O \cdots O–Cu contacts are formed. One of these contacts goes along the edge of the AsO_4 tetrahedron, while the second contact does not involve any bonds or polyhedra. Nevertheless, its short O \cdots O distance of $2.8 - 3.0$ Å is likewise beneficial for the superexchange. The resulting coupling $J_{id2} \simeq 140$ K is comparable to the typical interaction via double PO_4 and AsO_4 bridges in $\text{Sr}_2\text{Cu}(\text{PO}_4)_2$,⁴⁹ $\text{K}_2\text{CuP}_2\text{O}_7$,⁵⁰ and $\text{Cu}_2\text{As}_2\text{O}_7$.⁴⁸

Regarding the spin model of clinoclase, the “strong” (J) and “weak” (J_{D2}) magnetic dimers are joined into a planar structure (Fig. 8) by non-frustrated interdimer couplings J_{id1} and J_{id2} . Three interpenetrating planes of this type together form one structural “sandwich” and remain nearly decoupled. Topologically, each of the three lattices represents a diluted square lattice of magnetic dimers, depicted schematically in Fig. 8.

This spin lattice only marginally differs from a simple superposition of two nonequivalent dimers. The phenomenological “2+1” dimer model and the 2D spin lattice provide nearly indistinguishable fits of the magnetic susceptibility (Fig. 2). Field dependence of the magnetization, as calculated by QMC, is very close to the intuitive picture of isolated spin dimers (Fig. 9). The wide plateau at $M = \frac{1}{3}$ is due to the saturation of the “weak” dimers (J_{D2}), while the “strong” (J) dimers remain in the singlet state. Therefore, J_{id1} and J_{id2} have little effect

on the magnetic susceptibility of clinoclase.

The effect of these weak couplings is visible by comparing the magnetization curves simulated for isolated dimers and for the dimers coupled by J_{id1} and J_{id2} , as shown in Fig. 8. In the model augmented by J_{id1} and J_{id2} , the transitions preceding and following the $\frac{1}{3}$ -plateau are broadened compared to the “2+1” dimer model (Fig. 9). This broadening is caused by the interdimer couplings J_{id1} and J_{id2} that give rise to a dispersion of magnetic excitations, and mediate magnon-magnon interactions underlying the peculiar effect of spontaneous magnon decay.⁵¹

Clinoclase belongs to the family of gapped quantum magnets with nonequivalent spin dimers. In contrast to other systems of this type, different spin dimers are inherent to the crystal structure of this mineral. They are not formed due to a symmetry reduction upon a low-temperature phase transition that keeps similar magnetic interactions and, therefore, similar spin gaps in all dimers, as in BaCuSi₂O₆ (Ref. 5) and NH₄CuCl₃.⁶ Clinoclase can be rather compared to the ambient-pressure modification of (VO)₂P₂O₇, where two distinct spin gaps of 32 K and 65 K define two different energy scales of the system.^{52–54} Systems of this type may show interesting high-field behavior, because each group of dimers (J and J_{D2}) has independent low-temperature transitions related to the Bose-Einstein condensation (BEC) of magnons. The BEC transition takes place in the local field determined by the second group of dimers, either unpolarized J dimers for the BEC transition in J_{D2} , or polarized J_{D2} dimers for the BEC transition in J . Unfortunately, the critical fields of clinoclase (Fig. 9) are too high to observe such effects using present-day high-field facilities. Nevertheless, the search for similar systems with structurally different spin dimers should be an interesting avenue to explore the high-field physics of quantum magnets.

V. SUMMARY

In summary, we performed a joint theoretical and experimental study of the magnetic behavior of the mineral clinoclase. Using density functional theory calculations, we evaluate the microscopic model for this compound and

identify two types of spin dimers with the couplings of $J \simeq 700$ K and $J_{D2} \simeq 300$ K. Intuitively, one is tempted to ascribe them to two types of structural Cu₂O₆ dimers in clinoclase. In fact, only J_{D2} pertains to the structural dimer D2, while the strong coupling J occurs between two corner-sharing D1 dimers. Additional couplings between the magnetic dimers reach 150 K, but play a minor role in the magnetic behavior. Simulations for the DFT-based microscopic magnetic model yield excellent agreement with the experimental data.

The magnetic couplings in clinoclase are not solely determined by the Cu–O–Cu angles. The AsO₄ side groups and the hydrogen atoms also play an important role by enhancing or suppressing antiferromagnetic contributions to short-range couplings J_{D1} , J_{D2} , and J_{id1} . Since no hydrogen positions were available from the experiment, we determined them by optimizing the crystal structure within DFT. We have demonstrated that the magnetic coupling within D1 is strongly affected by the hydrogen atom attached to one of the bridging oxygens. The out-of-plane H position is responsible for the almost canceled exchange coupling J_{D1} . Our findings put forward details of the crystal structure, including inconspicuous and typically overlooked effects like hydrogen positions, as an important and even decisive factor in the magnetic superexchange.

ACKNOWLEDGMENTS

We are grateful to Gudrun Auffermann for her kind help with the chemical analysis. We also acknowledge the experimental support by Yurii Prots and Horst Borrmann (laboratory XRD), Yves Watier (ID31), and the provision of the ID31 beamtime by ESRF. We would like to thank the Department of Materials Engineering and Physics of the Salzburg University for providing the high-quality natural sample of clinoclase from their mineralogical collection (inventory number 14797). AT and OJ were supported by the European Union through the European Social Fund (Mobilitas Grants no. MTT77 and MJD447). SL acknowledges the funding from the Austrian Fonds zur Förderung der wissenschaftlichen Forschung (FWF) via a Schrödinger fellowship J3247-N16.

* altsirlin@gmail.com

† Helge.Rosner@cpfs.mpg.de

¹ R. J. Birgeneau, H. J. Guggenheim, and G. Shirane, *Phys. Rev. B* **1**, 2211 (1970).

² A. Epstein, E. Gurewitz, J. Makovsky, and H. Shaked, *Phys. Rev. B* **2**, 3703 (1970).

³ C. Zhou, D. P. Landau, and T. C. Schulthess, *Phys. Rev. B* **76**, 024433 (2007).

⁴ For example: H. M. Rønnow, D. F. McMorrow, and A. Harrison, *Phys. Rev. Lett.* **82**, 3152 (1999); P. A. God-

dard, J. L. Manson, J. Singleton, I. Franke, T. Lancaster, A. J. Steele, S. J. Blundell, C. Baines, F. L. Pratt, R. D. McDonald, O. E. Ayala-Valenzuela, J. F. Corbey, H. I. Southerland, P. Sengupta, and J. A. Schlueter, *ibid.* **108**, 077208 (2012).

⁵ D. V. Sheptyakov, V. Y. Pomjakushin, R. Stern, I. Heinmaa, H. Nakamura, and T. Kimura, *Phys. Rev. B* **86**, 014433 (2012); C. Rüegg, D. F. McMorrow, B. Normand, H. M. Rønnow, S. E. Sebastian, I. R. Fisher, C. D. Batista, S. N. Gvasaliya, C. Niedermayer, and J. Stahn, *Phys. Rev.*

- Lett. **98**, 017202 (2007); S. Krämer, R. Stern, M. Horvatić, C. Berthier, T. Kimura, and I. R. Fisher, Phys. Rev. B **76**, 100406(R) (2007).
- ⁶ C. Rüegg, M. Oettli, J. Schefer, O. Zaharko, A. Furrer, H. Tanaka, K. W. Krämer, H.-U. Güdel, P. Vorderwisch, K. Habicht, T. Polinski, and M. Meissner, Phys. Rev. Lett. **93**, 037207 (2004).
- ⁷ S. E. Sebastian, N. Harrison, C. D. Batista, L. Balicas, M. Jaime, P. A. Sharma, N. Kawashima, and I. R. Fisher, Nature **441**, 617 (2006); O. Rösch and M. Vojta, Phys. Rev. B **76**, 224408 (2007); N. Laflorencie and F. Mila, Phys. Rev. Lett. **107**, 037203 (2011).
- ⁸ W. Shiramura, K. Takatsu, B. Kurniawan, H. Tanaka, H. Uekusa, Y. Ohashi, K. Takizawa, H. Mitamura, and T. Goto, J. Phys. Soc. Jpn. **67**, 1548 (1998).
- ⁹ H. Inoue, S. Tani, S. Hosoya, K. Inokuchi, T. Fujiwara, T. Saito, T. Suzuki, A. Oosawa, T. Goto, M. Fujisawa, H. Tanaka, T. Sasaki, S. Awaji, K. Watanabe, and N. Kobayashi, Phys. Rev. B **79**, 174418 (2009).
- ¹⁰ B. Koteswararao, S. Salunke, A. V. Mahajan, I. Dasgupta, and J. Bobroff, Phys. Rev. B **76**, 052402 (2007); O. Mentré, E. Janod, P. Rabu, M. Hennion, F. Leclercq-Hugeux, J. Kang, C. Lee, M.-H. Whangbo, and S. Petit, *ibid.* **80**, 180413(R) (2009); A. A. Tsirlin, I. Rousochatzakis, D. Kasinathan, O. Janson, R. Nath, F. Weickert, C. Geibel, A. M. Läuchli, and H. Rosner, *ibid.* **82**, 144426 (2010).
- ¹¹ J. Deisenhofer, R. M. Eremina, A. Pimenov, T. Gavrilova, H. Berger, M. Johnsson, P. Lemmens, H.-A. K. von Nidda, A. Loidl, K.-S. Lee, and M.-H. Whangbo, Phys. Rev. B **74**, 174421 (2006).
- ¹² O. Janson, A. A. Tsirlin, J. Sichelschmidt, Y. Skourski, F. Weickert, and H. Rosner, Phys. Rev. B **83**, 094435 (2011).
- ¹³ M. Schmitt, A. A. Gippius, K. S. Okhotnikov, W. Schnelle, K. Koch, O. Janson, W. Liu, Y.-H. Huang, Y. Skourski, F. Weickert, M. Baenitz, and H. Rosner, Phys. Rev. B **81**, 104416 (2010).
- ¹⁴ E. E. Kaul, H. Rosner, V. Yushankhai, J. Sichelschmidt, R. V. Shpanchenko, and C. Geibel, Phys. Rev. B **67**, 174417 (2003); A. A. Tsirlin and H. Rosner, *ibid.* **83**, 064415 (2011); O. Janson, A. A. Tsirlin, E. S. Osipova, P. S. Berdonosov, A. V. Olenov, V. A. Dolgikh, and H. Rosner, *ibid.* **83**, 144423 (2011).
- ¹⁵ S. Ghose, M. Fehlmann, and M. Sundaralingam, Acta Cryst. **18**, 777 (1965).
- ¹⁶ R. K. Eby and F. C. Hawthorne, Acta Cryst. **C46**, 2291 (1990).
- ¹⁷ J. B. Goodenough, Phys. Rev. **100**, 564 (1955).
- ¹⁸ J. Kanamori, J. Phys. Chem. Solids **10**, 87 (1959).
- ¹⁹ P. W. Anderson, Solid State Phys. **14**, 99 (1963).
- ²⁰ ICP-OES (inductively coupled plasma optical emission spectrometry) analysis was performed with the VISTA instrument from Varian.
- ²¹ Measurements are done using a Netzsch STA 449C instrument with a Al₂O₃ crucible, argon gas and a gas flow of 120 ml/min.
- ²² K. Koepf and H. Eschrig, Phys. Rev. B **59**, 1743 (1999).
- ²³ J. P. Perdew and Y. Wang, Phys. Rev. B **45**, 13244 (1992).
- ²⁴ J. P. Perdew, K. Burke, and M. Ernzerhof, Phys. Rev. Lett. **77**, 3865 (1996).
- ²⁵ A. G. Petukhov, I. I. Mazin, L. Chioncel, and A. I. Lichtenstein, Phys. Rev. B **67**, 153106 (2003).
- ²⁶ A. A. Tsirlin, O. Janson, S. Lebernegg, and H. Rosner, Phys. Rev. B **87**, 064404 (2013).
- ²⁷ O. Janson, W. Schnelle, M. Schmidt, Y. Prots, S.-L. Drechsler, S. Filatov, and H. Rosner, New J. Phys. **11**, 113034 (2009).
- ²⁸ O. Janson, A. A. Tsirlin, M. Schmitt, and H. Rosner, Phys. Rev. B **82**, 014424 (2010).
- ²⁹ N. W. Winter, R. M. Pitzer, and D. K. Temple, J. Chem. Phys. **86**, 3549 (1987).
- ³⁰ D. Muñoz, I. de P. R. Moreira, and F. Illas, Phys. Rev. B **65**, 224521 (2002).
- ³¹ F. Neese, ORCA version 2.9, MPI for Bioinorganic Chemistry, Muhlheim a. d. Ruhr, Germany, 2011.
- ³² F. Neese, in *Biological Magnetic Resonance*, Vol. 28, edited by G. Hanson and L. Berliner (Springer, 2008) pp. 175–232.
- ³³ J. P. Perdew, M. Ernzerhof, and K. Burke, J. Chem. Phys. **105**, 9982 (1996); M. Ernzerhof and G. E. Scuseria, *ibid.* **110**, 5029 (1999).
- ³⁴ S. Todo and K. Kato, Phys. Rev. Lett. **87**, 047203 (2001).
- ³⁵ A. W. Sandvik, Phys. Rev. B **59**, 14157 (1999).
- ³⁶ A. Albuquerque, F. Alet, P. Corboz, P. Dayal, A. Feiguin, S. Fuchs, L. Gamper, E. Gull, S. Gürtler, A. Honecker, R. Igarashi, M. Körner, A. Kozhevnikov, A. Läuchli, S. R. Manmana, M. Matsumoto, I. P. McCulloch, F. Michel, R. M. Noack, G. Pawłowski, L. Pollet, T. Pruschke, U. Schollwöck, S. Todo, S. Trebst, M. Troyer, P. Werner, and S. Wessel, J. Magn. Magn. Mater. **310**, 1187 (2007).
- ³⁷ See Supplemental Material for details of the structure refinement, refined atomic positions, TGA data and hydrogen bonds within the *bc*-plane.
- ³⁸ www.mindat.org/min1055.html, “Clinoclase,” (2013).
- ³⁹ Note that we use plain LDA and GGA instead of the DFT+*U* methods, because strong correlations in the Cu 3*d* shell should not affect the O–H bonds and the positions of hydrogen.
- ⁴⁰ S. Lebernegg, O. Janson, A. A. Tsirlin, and H. Rosner, to be published.
- ⁴¹ LSDA+*U* calculations arrive at the band gap of about 2.6 eV in reasonable agreement with the blue color of clinoclase.
- ⁴² E. Ruiz, P. Alemany, S. Alvarez, and J. Cano, Inorg. Chem. **36**, 3683 (1997).
- ⁴³ S. Lebernegg, M. Schmitt, O. Janson, A. A. Tsirlin, and H. Rosner, Phys. Rev. B **XX**, (in press) (2013).
- ⁴⁴ M. Braden, G. Wilkendorf, J. Lorenzana, M. Aïn, G. J. McIntyre, M. Behruzi, G. Heger, G. Dhalenne, and A. Revcolevschi, Phys. Rev. B **54**, 1105 (1996).
- ⁴⁵ For example: A. Oosawa, T. Kato, H. Tanaka, K. Kakurai, M. Müller, and H.-J. Mikeska, Phys. Rev. B **65**, 094426 (2002).
- ⁴⁶ S. Miyahara and K. Ueda, J. Phys.: Cond. Matter **15**, R327 (2003); M. Takigawa, T. Waki, M. Horvatić, and C. Berthier, J. Phys. Soc. Jpn. **79**, 011005 (2010).
- ⁴⁷ W. Geertsma and D. Khomskii, Phys. Rev. B **54**, 3011 (1996).
- ⁴⁸ Y. C. Arango, E. Vavilova, M. Abdel-Hafiez, O. Janson, A. A. Tsirlin, H. Rosner, S.-L. Drechsler, M. Weil, G. Nénert, R. Klingeler, O. Volkova, A. Vasiliev, V. Kataev, and B. Büchner, Phys. Rev. B **84**, 134430 (2011).
- ⁴⁹ M. D. Johannes, J. Richter, S.-L. Drechsler, and H. Rosner, Phys. Rev. B **74**, 174435 (2006).
- ⁵⁰ R. Nath, D. Kasinathan, H. Rosner, M. Baenitz, and C. Geibel, Phys. Rev. B **77**, 134451 (2008).

- ⁵¹ M. E. Zhitomirsky and A. L. Chernyshev, *Rev. Mod. Phys.* **85**, 219 (2013).
- ⁵² T. Yamauchi, Y. Narumi, J. Kikuchi, Y. Ueda, K. Tatani, T. C. Kobayashi, K. Kindo, and K. Motoya, *Phys. Rev. Lett.* **83**, 3729 (1999); J. Kikuchi, K. Motoya, T. Yamauchi, and Y. Ueda, *Phys. Rev. B* **60**, 6731 (1999).
- ⁵³ U. Kuhlmann, C. Thomsen, A. V. Prokofiev, F. Büllersfeld, E. Uhrig, and W. Assmus, *Phys. Rev. B* **62**, 12262 (2000).
- ⁵⁴ D. C. Johnston, T. Saito, M. Azuma, M. Takano, T. Yamauchi, and Y. Ueda, *Phys. Rev. B* **64**, 134403 (2001).

Supporting Material

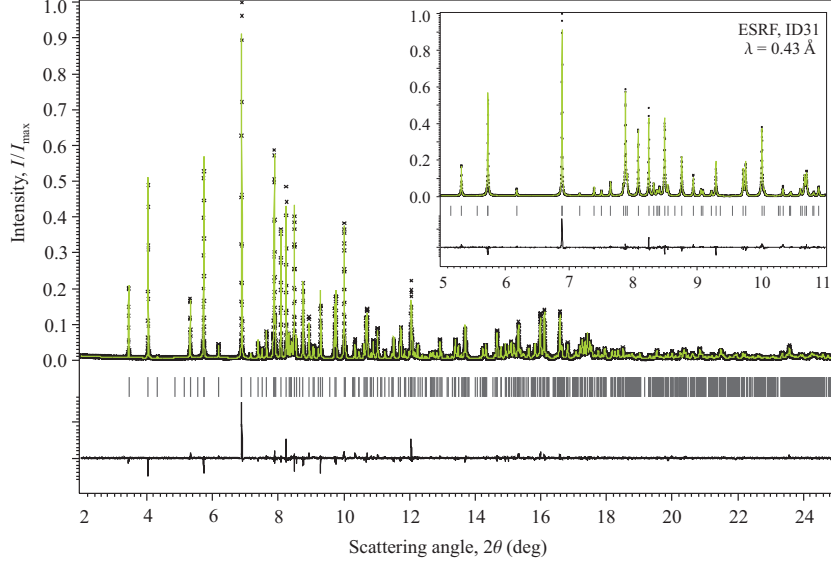


FIG. 10. Rietveld refinement of the room-temperature high-resolution XRD data. Ticks show the reflection positions of clinoclase.

TABLE III. The lattice parameters, atomic positions and atomic displacements parameters U_{iso} (in 10^{-2} \AA^2) refined from the high-resolution powder XRD data on the natural sample of clinoclase. Positions of hydrogen atoms are determined by a DFT-based structure optimization within GGA. All atoms are in the $4e$ Wyckoff position of the $P2_1/c$ space group.

Atom	x/a	y/b	z/c	U_{iso}
Cu1	0.7864(2)	0.1400(2)	0.3296(1)	0.74(3)
Cu2	0.8141(2)	0.3802(2)	0.1272(1)	0.77(3)
Cu3	0.3856(2)	0.3527(2)	0.4120(1)	0.99(4)
As	0.3083(1)	0.1509(2)	0.1794(1)	0.85(3)
O1	0.4090(7)	0.0712(8)	0.0714(4)	0.14(6) ^a
O2	0.8387(7)	0.8447(8)	0.3681(4)	0.14(6) ^a
O3	0.1802(7)	0.9408(8)	0.2108(4)	0.14(6) ^a
O4	0.4705(8)	0.2147(7)	0.2813(4)	0.14(6) ^a
O5	0.7777(7)	0.2039(7)	0.4780(4)	0.14(6) ^a
O6	0.8047(7)	0.0957(8)	0.1747(4)	0.14(6) ^a
O7	0.1871(7)	0.1705(8)	0.4157(4)	0.14(6) ^a
H1 ^b	0.7493	0.3515	0.4807	–
H2 ^b	0.9346	0.4680	0.6787	–
H3 ^b	0.1511	0.1648	0.4864	–

^a The atomic displacements parameters of all oxygen atoms were refined as a single parameter

^b Hydrogen positions are obtained from the structure relaxation within GGA

TABLE IV. The t_{D1} and t hopping parameters (in meV) as function of the out-of-plane angle of H, τ . $U_{\text{eff}} = 4.0$ eV in the AFM exchange contributions J_{D1}^{AFM} (in K). The ferromagnetic contribution is defined as $J_{D1}^{\text{FM}} = J_{D1} - J_{D1}^{\text{AFM}}$. J_{D1} (in K) is calculated with the $\text{Cu}_2\text{O}_6\text{H}_5$ cluster model and a PBE0 hybrid functional.

τ	t_{D1}	t	J_{D1}^{AFM}	J_{D1}^{FM}	J_{D1}
7	-186	292	401	213	188
11	-184	289	393	208	185
22	-169	283	331	174	157
31	-155	281	279	161	118
39	-144	278	241	163	78
52	-128	276	190	175	15
67	-115	276	153	183	-30

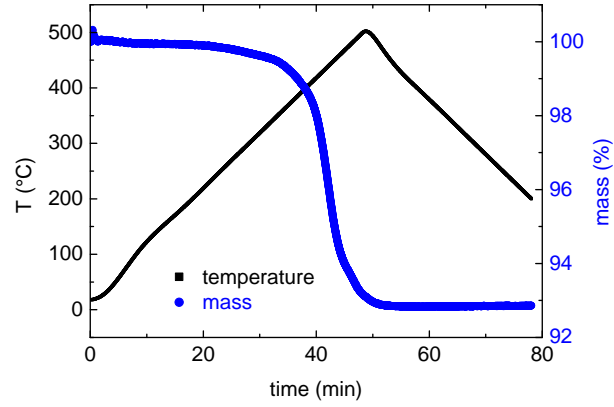


FIG. 11. (Color online) Thermogravimetric analysis data taken in a temperature range of 20–500 °C. The mass loss amounts to 7.13%.

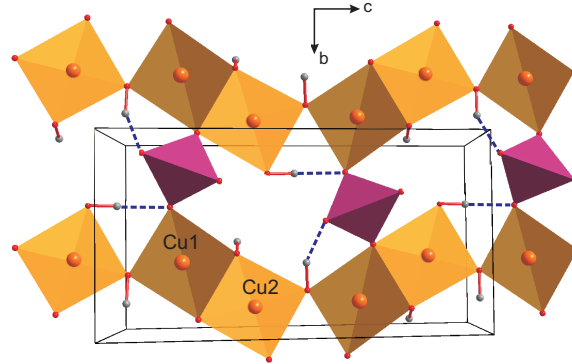


FIG. 12. (Color online) The hydrogen bonds (blue) within the bc -plane of the clinoclase structure. The D1 dimers are shown in orange and the AsO_4 tetrahedra in pink color.